

Quantification of Flow Noise Produced by an Oscillating Foil

Muhammad Saif Ullah Khalid^{1,2}, Xiaoping Jiang¹, Imran Akhtar², Binxin Wu¹

¹Research Center for Fluid Machinery Engineering and Technology, Jiangsu University, Zhenjiang, 212013, Jiangsu, People's Republic of China.

²Department of Mechanical Engineering, College of Electrical & Mechanical Engineering, National University of Sciences & Technology, Rawalpindi, 46000, Pakistan.

E-mail: mskhalid1984@gmail.com

‡

June 2018

Abstract. Getting inspired from swimming natural species, a lot of research is being carried out in the field of unmanned underwater vehicles. During the last two decades, more emphasis on the associated hydrodynamic mechanisms, structural dynamics, control techniques and, its motion and path planning has been prominently witnessed in the literature. Considering the importance of the involved acoustic mechanisms, we focus on the quantification of flow noise produced by an oscillating hydrofoil here employed as a kinematic model for fish or its relevant appendages. In our current study, we perform numerical simulations for flow over an oscillating hydrofoil for a wide range of flow and kinematic parameters. Using the Ffowcs-Williams and Hawkings (FW-H) method, we quantify the flow noise produced by a fish during its swimming for a range of kinematic and flow parameters including Reynolds number, reduced frequency, and Strouhal number. We find that the distributions of the sound pressure levels at the oscillating frequency and its first even harmonic due to the pressure fluctuations in the fluid domain are dipole-like patterns. The magnitudes of these sound pressure levels depend on the Reynolds number and Strouhal number, whereas the direction of their dipole-axes appears to be affected by the reduced frequency only. Moreover, We also correlate this emission of sound radiations with the hydrodynamic force coefficients.

Keywords: Flow Noise, Acoustics, Fish-swimming, Oscillating Foil

1. Introduction

Since the advent of unmanned swimming robots, underlying hydrodynamic mechanisms for producing the required forces for propulsion and other movements have attracted the attention of researchers from diverse backgrounds. These belong

‡ This file is produced using the IOPScience LaTeX class.

to fluid mechanics, fluid-structure interaction, dynamics and control, and now machine vision etc. Extensive research work in all these fields have been reported in the literature [1–6]. However, this work lacks dedicated efforts in quantification of flow noise produced by such vehicles. It is particularly relevant for their prospective application to perform missions silently in the hostile environments. This study is also important in exploring the mechanisms adopted by fishes to feel the presence of other objects around them. They may utilize these signals for various biological motives such as behavioral communication and navigation in a certain environment. It is also interesting to examine the dependence of directionality in sound emission on flow properties and body-kinematics. Many biologists have presented their work on sounds produced by fish for their social and behavioral motives [7]. Also, they focused on investigating the hearing mechanisms utilized by different fishes. There were only a few studies in literature devoted to the quantification of sound produced by oscillating bodies [8–12]. These pieces of work concentrated on the noise production in air by flying species. Sueur et al. [8] characterized the acoustic radiations from the flapping appendages of a blowfly through close-range recordings. They found out that the sound spectrum contained a series of frequencies. They also observed that the sound pressure levels at first harmonic showed a dipole like structure in the horizontal plane of the fly, whereas second harmonic came out with a monopole like radiation pattern. In their case, fundamental harmonic was more dominant in the upstream direction of the fly, and second harmonic showed more dominance in the sideways. Their recordings in the downstream direction of the specie corresponded to a broadband noise that was termed as the pseudo-sound. They remarked that the pseudo-sounds were produced from the vortices in the wake of the flying object. Bae et al. [9] performed numerical simulations for flow around a two-dimensional (2D) model of another flying insect in hovering and forward flight conditions. They determined two sound production mechanisms with dipole tones due to the traversing wing-motion and vortex edge scattering during a tangential motion. They argued that the primary tone with the wing beat frequency is directional for hovering motion, and it showed monopole like character for forward flight. For hovering, they also associated the tonal frequencies with those of the fluid force coefficients, but the question of directionality for forward flight remained unclear. Similarly, Inada et al. [10] also carried out three-dimensional (3D) simulations to uncover the mechanisms for sound production by the flapping wings of three insects; hawkmoth, honeybee, and fruitfly. They concluded that flapping sound was dependent on amplitude, frequencies, and the observer's position. They also found the fundamental harmonic as the dominant one. The experimental work done by Lu et al. [11] on the flapping sound of a robot using flapping wings uncovered that a highly elastic material could reduce the flapping noise to a great extent. A more dedicated effort in this direction was recently done by Geng et al. [12]. They performed numerical simulations using a hydrodynamic/acoustic splitting approach, where acoustic field is modeled through linearized perturbed compressible equations. Their simulations revealed the directionality of sound, and reduction of flapping sound with an enhanced flexibility of wings. Additionally, they argued that

the fundamental harmonic in the sound spectra dominates in the direction of the stroke plane, and in the downstream direction for rigid and flexible wings, respectively. In their case, second harmonic showed more strength sideways for rigid wing, and towards left and upper sides for the flexible wings. They also explored that the direction of the dipole axis was different for rigid and flexible wings. The sound emission and its propagation was found to be highly associated with the wing loading. Up to the authors' knowledge, no concerted effort to investigate the noise produced in water by fish-bodies has been seen in the literature. Also, the dependence of the sound pressure levels on various key parameters has not been explored. Still, there are unanswered questions regarding the sound production and propagation from the oscillating body-structures which are more specific to fish swimming. These factors include the effect of flow parameters such as Reynolds number (Re) and the wake-width resulted due to vortices shed from the trailing-edge of the bodies, and the kinematic parameters like oscillation/excitation frequency (f_E) and amplitude etc. These aspects motivate our current research work. This study will assist in understanding the mechanisms adopted by fish to avoid predators, and to propose better designs for unmanned underwater robots to perform their missions silently, and without being noticed by the surrounding hostilities.

In this study, we focus on quantifying the flow noise as the sound pressure levels measured in dB that is produced by the oscillatory motion of fish bodies, or their relevant appendages during swimming. As the hydrodynamic flow characterization for oscillating bodies depends on three similarity parameters; the Reynolds number ($Re = \frac{\rho U_\infty c}{\mu}$), the reduced frequency ($k = \frac{f_E c}{U_\infty}$), and the Strouhal number ($St = \frac{f_E A}{U_\infty}$) [13], the results may be considered as applicable to the other oscillatory systems operating with the same range of these parameters. Here, ρ , μ , c and U_∞ show the fluid-density, dynamic viscosity of the fluid, chord-length, and free-stream fluid-velocity, respectively. The amplitude A is the maximum amplitude traversed by the trailing-edge of the hydrofoil, and a measure of the wake-width for reverse von Karman vortex street. We carry out numerical simulation for flow over an oscillating hydrofoil structure, a representative of fish-body or its fin, for $Re = 5,000, 10,000, \text{ and } 20,000$. We vary the St ranging from 0.10 to 0.50 that is a usual range of fish swimming for efficient hydrodynamic performance [13]. We also set k equal to 1, 2.5, and 5 which represent its low, moderate, and high values, respectively.

2. Numerical Methodology

2.1. Hydrofoil Kinematics

We model a fish-body, or its single fin using a hydrofoil having circular leading-edge with $D/c = 0.06$ [2]. Governing mathematical relation for its kinematics is given below.

$$\theta(t) = \theta_\circ \sin 2\pi ft \quad (1)$$

where $\theta(t)$ is the instantaneous angular position of the hydrofoil, θ_0 is its maximum excursion from its mean position, and t denotes the time in seconds. This hydrofoil conducts pitching motion about its leading-edge.

2.2. Flow Solver

To perform our numerical simulations, we use ANSYS Fluent 16.1 [14], a commercial finite volume based computational platform, that has gained a lot of popularity among researchers for several fluid flow simulations [15–17]. Incompressible unsteady Reynolds-averaged continuity and Navier-Stokes (URANS) equations in Cartesian coordinates, given as 2 and 3, respectively, in tensor form, are solved through the pressure-based solver.

$$\frac{\partial u_j}{\partial x_j} = 0 \quad (2)$$

$$\frac{\partial u_i}{\partial t} + \frac{\partial}{\partial x_j}(u_i u_j) = -\frac{1}{\rho} \frac{\partial p}{\partial x_i} + \nu \frac{\partial^2 u_i}{\partial x_j \partial x_j} \quad (3)$$

where x_j denotes the Cartesian coordinates, and $j = \{1, 2\}$. u shows the Cartesian velocity components, ρ is the water density here, p shows the pressure, and ν indicates the kinematic viscosity. Due to the absence of a pressure term in the Continuity equation (see 2), semi-implicit method for pressure linked equations (SIMPLE), semi-implicit method for pressure linked equations-consistent (SIMPLEC), pressure implicit with splitting operators (PISO), and Coupled algorithms [14] are provided in the solver. Although PISO is recommended for unsteady flows [18], it is usually advantageous when a large time-step (Δt) is adopted to computationally march in time. Hence, to improve the computational efficiency, we adopt SIMPLE algorithm for our cases.

We utilize the Green-Gauss cell based technique for computation of the gradient terms, the second order scheme for the convective pressure terms, and the higher order Quadratic Upstream Interpolation for Convective Kinematics (QUICK) scheme for the diffusion terms in the momentum equation (3). The unsteady term is approximated by the second order implicit scheme. We perform the unsteady simulations through the sliding mesh technique that allows physical pitching motion of the hydrofoil without disturbing the original mesh.

To use higher order schemes for numerical approximation of temporal term, [15, 17, 19–21] proposed employment of sliding mesh technique that was also followed by other researchers like Ashraf et al. [16, 22]. In this technique, pitching airfoil is placed in a heaving reference frame by applying the time-varying velocity condition at the inlet boundary, as shown in figure 1. It serves as the relative velocity of the reference frame with respect to the airfoil. The pitching motion of the airfoil is attributed to defining a separate zone around it through non-conformal sliding mesh circular interface. Although this method is computationally more expensive for handling moving reference frame in

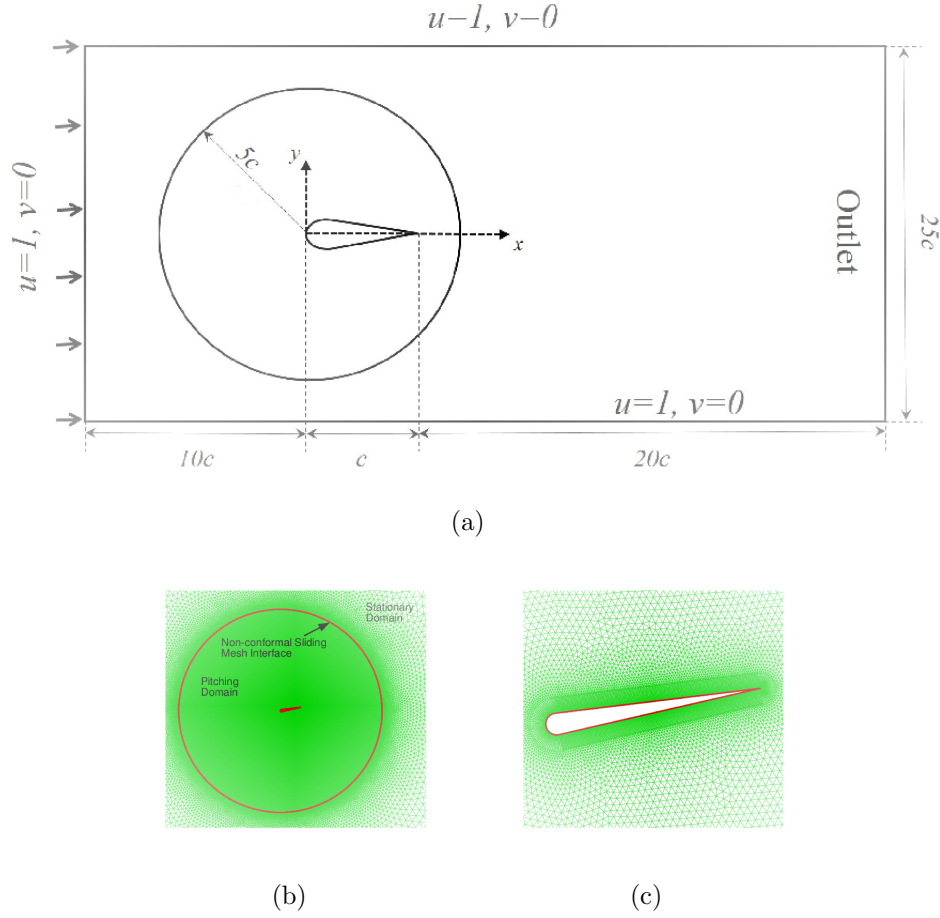


Figure 1. (a) Schematic of computational domain and details of the boundary conditions, (b) non-conformal sliding interface between the stationary and the pitching zones, and (c) mesh density around the whole surface of the airfoil

flow-fields, yet it provides most accurate simulation methodology because it ensures the maintainability of a higher quality mesh provided to the solver initially.

To avoid effects of the disturbances on the boundaries of the computational domain, the inlet boundary is placed at a distance of $10c$ from the leading-edge of the hydrofoil, while the top and bottom boundaries are $12.5c$ units away from the foil. The outlet boundary is kept at a distance of $20c$ from the hydrofoil's trailing-edge. The radius of the inner pitching domain defining the boundary for the non-conformal sliding interface, is $5c$ as presented in figure 1(a). A zoomed-in view of the pitching zone is presented in figure 1(b). Flow domain is meshed using unstructured triangular cells. 550 nodes are present on hydrofoil surface while maintaining $y^+ \sim 1$. To fully capture the features of boundary layer flow, 14 arrays of the mesh-nodes are placed around the foil as shown in figure 1(b).

The convergence criterion for the iterative solution at each time-step is set to be 1×10^{-5} . Although we obtain convergence with almost 10 – 15 iterations at each time-step, maximum allowable number of iteration are 50. We run all the simulations for 10

oscillations where the steady-state solution is approached within 2 – 3 oscillation cycles, and provide the statistical quantities based on the data of the last 7 oscillations.

2.3. Acoustic Modeling

In this paper, we model the acoustics features using the Ffowcs-Williams and Hawkings (FW-H) method [23]. Having its roots in the earlier work by Lighthill [24], FW-H model predicts the sound generated by arbitrarily moving rigid bodies. Lighthill's fundamental analogy is derived from the continuity (2) and momentum equations (3) of fluid mechanics. FW-H model essentially presents an inhomogeneous wave equation [14, 23, 25, 26] as given below.

$$\frac{1}{a_{\circ}^2} \frac{\partial^2 p'}{\partial t^2} - \nabla^2 p' = \frac{\partial^2}{\partial x_i \partial x_j} \{T_{ij} H(f)\} - \left(\frac{\partial}{\partial x_i} \{[P_{ij} n_j + \rho u_i (u_n - v_n)] \delta(f)\} \right) + \left(\frac{\partial}{\partial t} \{[\rho_{\circ} v_n + \rho (u_n - v_n)] \delta(f)\} \right) \quad (4)$$

where u_i , u_n are the fluid Cartesian velocity components in x_i direction, and normal to the integration surface ($f = 0$), respectively. v_n is the velocity of the integration surface normal to the surface. $\delta(f)$ and $H(f)$ denote the Dirac Delta and Heavyside functions, respectively. p shows the sound pressure level in the far-field, and T_{ij} represents the Lighthill's stress tensor. The unit normal vector n_i points towards the exterior region ($f > 0$), and a_{\circ} denotes the speed of sound in the concerned physical medium. The subscript \circ indicates the free-stream quantities, and the primed quantities shows the difference between the values in the real domain and the undisturbed medium [26]. A mathematical surface ($f = 0$) is introduced to investigate the exterior flow phenomenon ($f > 0$) in an unbounded space. The surface $f = 0$ defines the shape and motion of the source surface which is the hydrofoil in the present case. $f > 0$ corresponds to the interior of the source surfaces. The terms of the right hand side in 4 models various source terms for sound generation. The Lighthill stress tensor, T_{ij} , the first source term, is defined as,

$$T_{ij} = \rho u_i u_j + P_{ij} - a_{\circ}^2 (\rho - \rho_{\circ}) \delta_{ij} \quad (5)$$

where P_{ij} shows the compressive stress tensor; a combination of the surface pressure (p) and the viscous stress.

$$P_{ij} = p \delta_{ij} - \mu \left\{ \frac{\partial u_i}{\partial x_j} + \frac{\partial u_j}{\partial x_i} - \frac{2}{3} \frac{\partial u_k}{\partial x_k} \delta_{ij} \right\} \quad (6)$$

The source modeled by the Lighthill stress tensor is known as quadrupole, where $H(f)$ depicts volume distribution of sources in the outer domain. The second term in 4 models the distribution of dipoles resulting from the unsteady external forces produced

due to the fluid-structure interaction. Last term here describes the distribution of monopoles generated from displacement of the fluid as a result of structural motion. The distributions of monopole, dipole, and quadrupole are also known as thickness noise, loading noise, and turbulence-induced noise, respectively. Basically, these are surface distribution sources as identified by the presence of the function $\delta(f)$ in the relevant terms of 4. The inhomogeneous wave equation (4) can be integrated analytically assuming the free-space flow, and the absence of obstacles between the sound sources and the receivers. The surface integrals gives contribution from the monopoles and dipoles sources and partially from quadrupole sources. The volume integrals denote quadrupole sources in the region outside the source surface. In case of very low Mach number flows ($M \ll 1$) such as the present fluid flow phenomenon, volume integrals do not contribute much towards quantification of noise. Hence, these terms can be neglected in further computations. Resultantly, we decompose the acoustic pressure (p') as follows.

$$p'(\vec{x}, t) = p'_T(\vec{x}, t) + p'_L(\vec{x}, t) \quad (7)$$

where \vec{x} represents the receiver's position, t is the observer time, whereas T and L denote the quantities associated with the thickness noise, and the loading noise, respectively. Then, we have [26,27],

$$4\pi p'_T(\vec{x}, t) = \int_{f=0} [\frac{\rho_o(\dot{U}_n - U_{\dot{n}})}{r(1 - M_r)^2}]_{ret} dS - \left(\int_{f=0} [\frac{\rho_o U_n (r\dot{M}_r + a_o(M_r + M^2))}{r^2(1 - M_r)^3}]_{ret} dS \right) \quad (8)$$

and

$$4\pi p'_L(\vec{x}, t) = \frac{1}{a_o} \int_{f=0} [\frac{\dot{L}_r}{r(1 - M_r)^2}]_{ret} dS + \left(\int_{f=0} [\frac{L_r - L_M}{r^2(1 - M_r)^3}]_{ret} dS \right) - \left(\frac{1}{a_o} \int_{f=0} [\frac{L_r (r\dot{M}_r + a_o(M_r + M^2))}{r^2(1 - M_r)^3}]_{ret} dS \right) \quad (9)$$

where

$$U_i = v_i + \frac{\rho}{\rho_o}(u_i - v_i) \quad (10)$$

$$L_i = P_{ij}\hat{n}_j + \rho u_i(u_n - v_n) \quad (11)$$

The subscripted quantities in 8 and 9 show the inner products of a vector and a unit vector denoted by the subscript. For example, $L_r = \vec{L} \cdot \vec{r}$, and $U_n = \vec{U} \cdot \vec{n}$, where \vec{r} , and \vec{n} are the unit vectors in the radial and normal direction to the wall boundary, respectively. The dot over a symbol represents the source-time differentiation of that

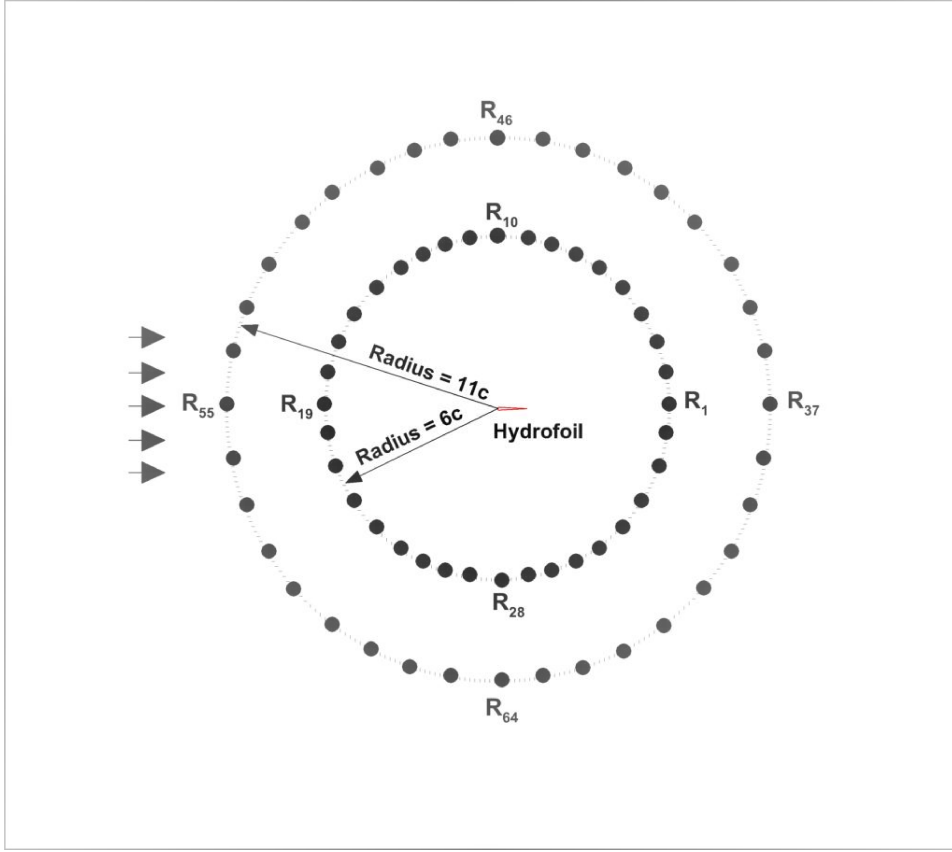


Figure 2. Schematic for the placement of acoustic receivers around the oscillating body

certain variable. The Mach number (M_i) denotes the ratio of the local surface velocity and the free-stream speed of sound in the relevant medium. The subscript (*ret*) shows that evaluation of the integrand at the retarded time (τ). With t as the observer/receiver time, and r as the distance to the receiver, it is defined as [26, 27],

$$\tau = t - \frac{r}{a_o} \quad (12)$$

We record the pressure fluctuations through placement of 72 acoustic receivers in the surroundings of the hydrofoil as shown in figure 2. Due to the spherical propagation (circular in case of 2D) of sound from its source, we select two locations to define circles used for the distribution of these probes. The distance of these receivers from the pitching-axis of the fish leading-edge are taken as $x/c = 6$ and 11. This positioning of receivers helps determine the directionality in propagation of the sound waves. The receivers are placed at these distances to allow the wake to settle down, and to avoid the recording of the pseudo-sound generated due to the transitional wake very close to the oscillating body. The flow noise caused due to the complex interaction between the near-field flow structures is termed as pseudo-sound [12].

Table 1. Results for grid and time-step convergence study at $St = 0.50$ and $k = 1$

Re	Grid	No. of Elements	Time-steps per oscillation cycle \bar{C}_T	
4700	Fine (G_1)	393675	2000	0.7251
4700	Medium (G_2)	191515	2000	0.7156
4700	Coarse (G_3)	94975	2000	0.7103
20000	Fine (G_1)	401110	4000	0.7251
20000	Fine (G_1)	401110	2000	0.7251
20000	Medium (G_2)	226722	2000	0.7156
20000	Coarse (G_3)	99840	2000	0.7103

2.4. Performance Parameters

To measure the hydrodynamic performance of the oscillating hydrofoil, we compute non-dimensional side-force coefficients, denoted as C_Y , C_D and C_M respectively, for all the cases. These coefficient are defined as,

$$\begin{aligned}
 C_Y &= \frac{F_Y}{qc} \\
 C_D &= \frac{F_D}{qc} \\
 C_M &= \frac{M}{qc^2}
 \end{aligned} \tag{13}$$

where F_Y , F_D , and M denote the side-force, drag, and moment, respectively. c is the chord length of the hydrofoil, and $q = \rho U_\infty^2 / 2$ represents the dynamic pressure. Using the time-period ($\tau = 1/f_E$) of one pitching cycle, corresponding time-averaged coefficients are computed using the following relation;

$$\bar{C} = \frac{1}{\tau} \int_t^{t+\tau} C(t) dt \tag{14}$$

2.5. Grid & Time-step Convergence Study

Due to the involvement of different Reynolds numbers in our present study, we perform grid independence study on $Re = 5000$ and 20000 . We compute the hydrodynamic coefficients for the lift (C_Y) equal to the side-force presently, thrust (C_T), and moment (C_M) for three configurations of different mesh sizes. The magnitude of the thrust force is equal to the drag, but these are in opposite directions. We characterize these configurations as G_1 (fine), G_2 (medium), and G_3 (coarse) as shown in Table 1. It also presents \bar{C}_T for these grids. As the appropriate time-step size is a function of the oscillation frequency in such scenario, we use 2,000 and 4,000 time steps in one oscillation cycle to check its convergence. The results reported in Table 1 show reasonable convergence of \bar{C}_T .

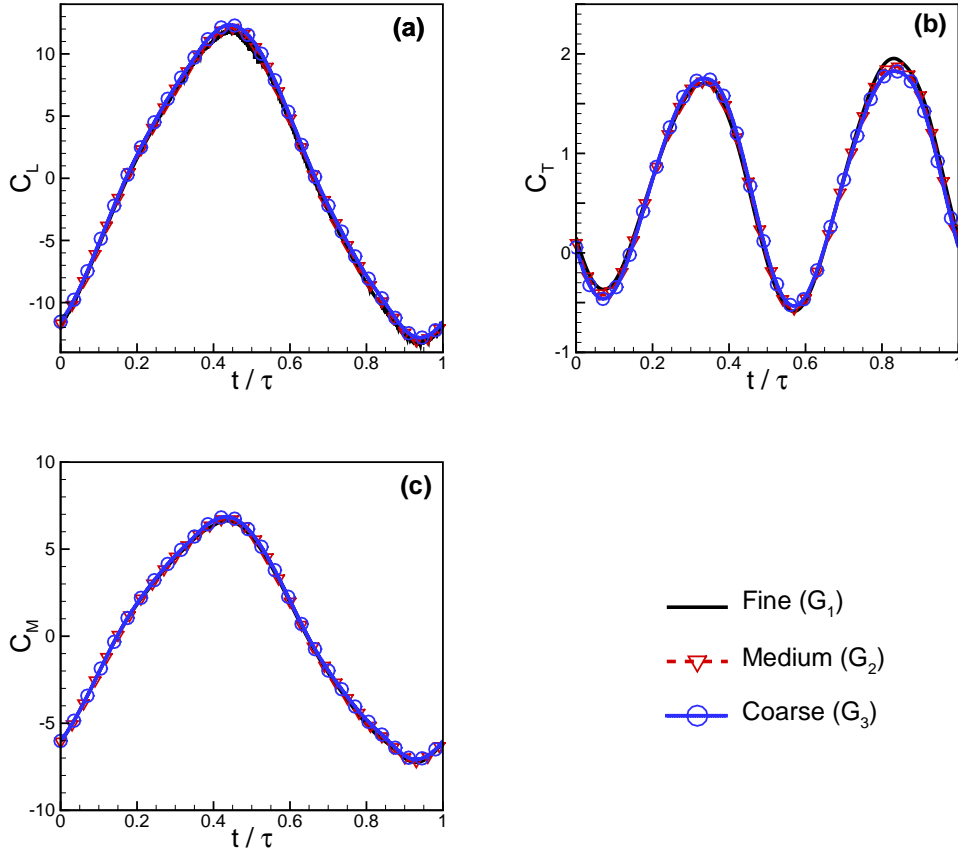


Figure 3. Results of the grid independence study for $Re = 5,000$

Moreover, we also present the temporal profiles of C_L , C_T , and C_M in figure 3 and 4 for all the grids and time-step sizes for $Re = 5,000$ and $20,000$, respectively. We adjust the grids near the hydrofoil to keep $y^+ = 1$ for different Re so that the boundary layer flow features may be appropriately resolved. We also show the time-averaged velocity magnitudes (V/U_∞) in the wake of oscillating hydrofoil at a distance of $x/c = 2$ and 3.5 in figure 5. These trends show a very small difference in the profiles obtained for G_1 and G_2 . Hence, we employ G_2 grid with 2,000 time-steps per oscillation cycle for our further simulations.

2.6. Validation

To validate our current numerical strategy, we compare the time-averaged thrust coefficients for a range of Strouhal number with those reported by Boschitsch et al. [2]. In this reference study, the same geometrical configuration for hydrofoils was used in a water tunnel to examine the hydrodynamic performance of their in-line arrangement. Here, we set $k = 1$, $Re = 4.7 \times 10^2$, and St varies from 0.10 to 0.50 with an interval of 0.05. Figure 6 shows the comparison between \bar{C}_T for both the studies. It provides a

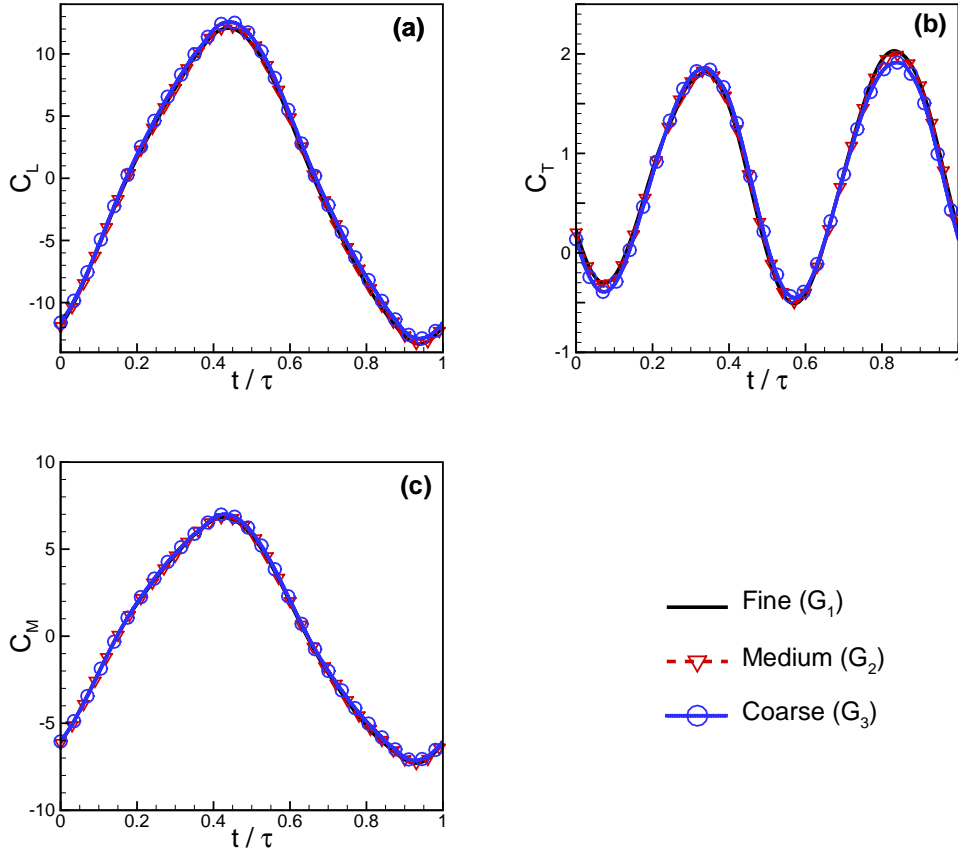


Figure 4. Results of the grid independence study for $Re = 20,000$

good indication for the accuracy of our simulation methodology.

3. Results & Discussion

In this study, we run all the simulations for 10 oscillation cycles while utilizing the data for the last 7 oscillation cycles for the computation of acoustic features after achieving the steady-state in the solution of the governing equations. We record the acoustic pressure signals at the designated receivers/probes, and process them with the Fourier transform technique (FFT) to extract the frequencies and their contribution towards the generation of these signals. Next, we use the reference pressure ($p_{ref} = 1 \times 10^{-6}$ Pa) for the conversion of the amplitude of all these frequency components into the sound pressure levels, commonly known as SPL. The reference pressure usually indicates the minimum sound pressure a human ear can sense at a certain frequency in water. Here, the role of Re , St , and k is quantified for the radiation of flow noise and its directivity caused by the oscillating fish-like hydrofoil.

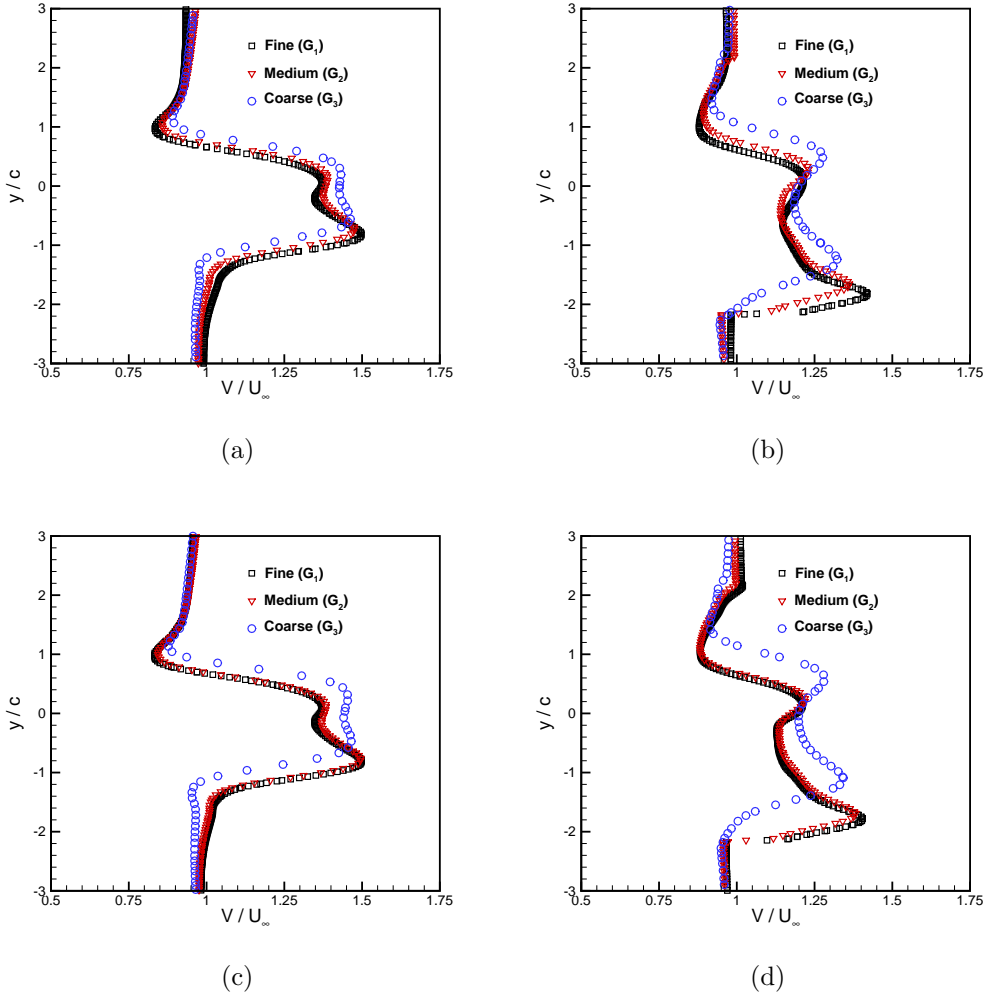


Figure 5. Nondimensional time-averaged velocity profiles in the wake of oscillating hydrofoil, (a) and (b) are computed at $Re = 5,000$, whereas (c) and (d) show corresponding values for $Re = 20,000$. Left column present values at a distance of $x/c = 2.0$ from the trailing-edge of the hydrofoil, and the right column here show data for the same at $x/c = 3.5$.

3.1. Emission of Sound Radiations

We perform our current numerical simulations for $Re = 5,000$, $10,000$, and $20,000$ while varying k with values of 1, 2.5, and 5. These values represent lower, middle and higher range of their associated parameters in hydrodynamics of aquatic species. We also set St ranging from 0.1 to 0.50 which are usually employed by natural species for swimming to achieve more efficient performance [13]. Figure 7 shows a representative schematic at $Re = 20,000$, $k = 5$, and $St = 0.50$ for computation of SPL at the probes of the inner circle around the pitching body. Fourier spectra for SPL comes out to be broad-band for the higher range of frequencies in all the cases. It is also interesting to observe that the forcing frequency has the most dominant component even in the

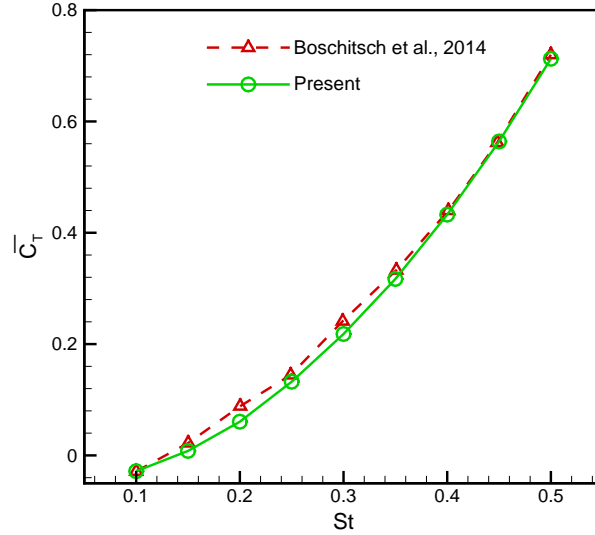


Figure 6. Comparison of \bar{C}_T from the present simulations, and experiments conducted by Boschitsch et al. [2] in a water tunnel

upstream direction of the flow. Additionally, these spectra reveal the propagation of pressure disturbance in all the directions, just like observed previously for the other flying species [9, 10, 12]. Depending on the sensitivity of the hearing parts of the surrounding bodies, the presence of a fish may be potentially detected by them. Additionally, it is only along the horizontal direction where the strength of the broadband noise in the spectra appears to be almost of the order of that of the forcing frequency and its first even harmonic.

To uncover the spectral features in more detail, we show a zoomed-in view of these plots in figure 8. It is obvious that the forcing frequency (f_E) and its first even harmonics at $2f_E$ play the strongest role in emission of the flow noise. Their significance also lies in the fact that these two frequency components are the strongest in the constitution of the hydrodynamic side-force and the drag/thrust force, respectively, to be discussed later in section 3.2. This trend is evidently seen for all the receivers. For the sake of brevity, we do not show the higher range of frequencies that constitutes the broadband noise in the latter part of these spectra. Some of the higher frequencies have SPL levels below zero which shows that the associated pressure is less than the reference sound pressure potentially causing difficulty in sensing such frequencies. These observations are valid for the whole range of governing kinematic and flow parameters used for our present investigations.

We show a comparison for the measurements in SPL for receivers placed at the inner and outer circles at a distance of $6c$ and $11c$ from the pitching-axis locations, respectively, in Figure 9. These sound signals tend to dissipate quickly as they traverse in the surroundings. The parameters, $k = 5$ and $St = 0.50$, here represent the strongest

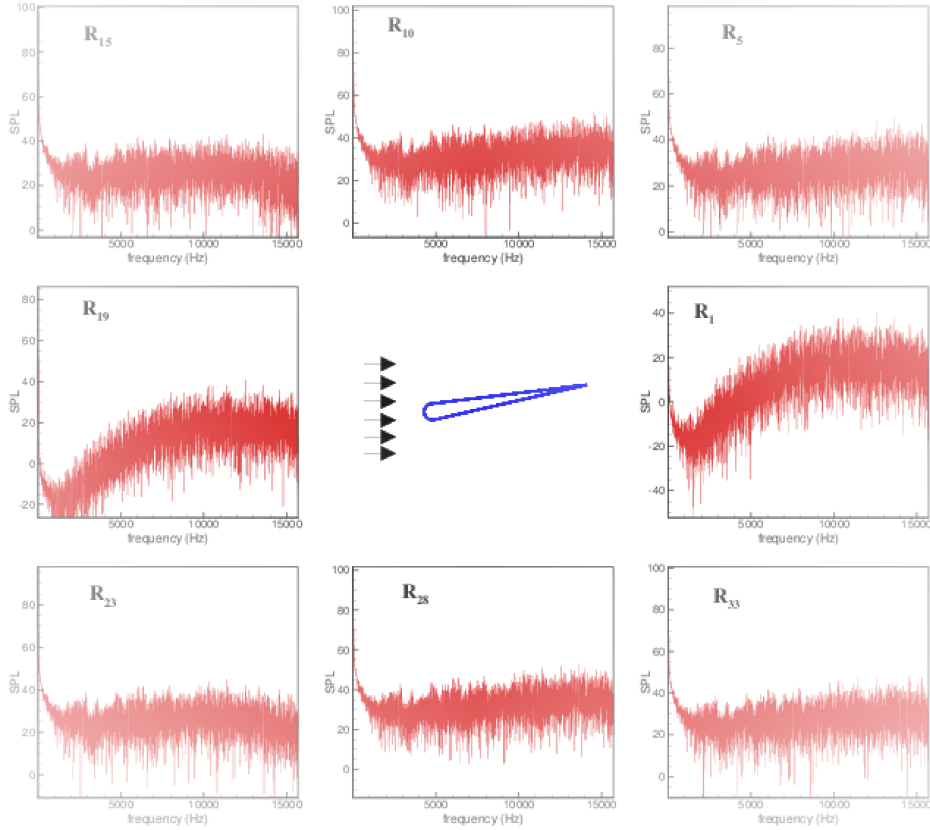


Figure 7. Frequency composition of SPL around the pitching hydrofoil at 8 locations in the circle closest to the body

disturbance in the flow media both in terms of oscillation amplitude and frequency. All the polar plots are drawn on the same scale for ease in comparison. With increasing Re , the SPL grows for both the frequencies, f_E and $2f_E$. We also notice that the propagation of sound radiations depicts the pitching body as a dipolar sound source for both the most dominant frequencies. As we move away from the body, the magnitudes of SPL get reduced for both the frequencies. Relying on such findings, our further discussion is based on the results computed at the receivers placed on the inner circle. Regarding the pattern of sound propagation, it is a dipole-like structure for f_E and $2f_E$. Although the peak-valley difference in this pattern for $2f_E$ is smaller as compared to that for f_E , yet the axis direction is clearly identified. Our observations for the SPL patterns are in agreement with those of [12]. It is revealed that the f_E dominates the sound spectra in all the directions, except along the horizontal axis. This trend persists for all the parameters considered presently.

Moreover, we find that the dipole axis for SPL at f_E remains horizontal for the whole range of Re , k , and St . None of these parameters affect the direction of this dipole axis. However, the dipole axis for SPL at $2f_E$ is sensitive to these parameters, and changes its angular position. To inspect it further, we extract and present the polar plots for SPL distributions for a range of all the governing parameters in figure 10. The SPL

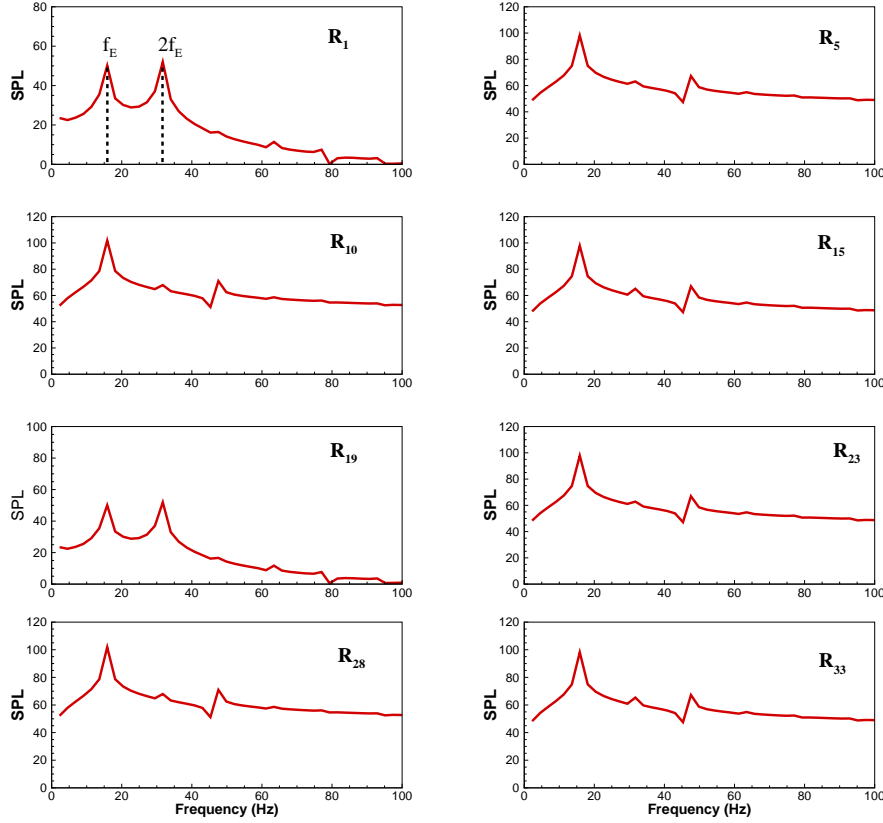


Figure 8. Frequency composition of SPL around the pitching hydrofoil at 8 locations in the circle closest to the body

radiation pattern in figure 10a for $k = 1$, $St = 0.15$ and $Re = 20,000$, and in figure 10f for $k = 2.5$, $St = 0.45$, and $Re = 20,000$ possess a negligible peak-valley difference, but a slight deviation in these dictating parameters provides evidence that these are essentially a representation of dipole-like structures. Contrary to our observations here, Geng et al. [12] opined that these kind of pattern looked like a monopole. Here, we support our argument by the parametric study revealing the dipolar nature of the SPL radiations at $2f_E$ in case of oscillating bodies for a wide range of governing k , St , and Re . It may need more investigations whether even larger Re may convert these dipole-like SPL distributions into monopole-like ones. Furthermore, these plots also manifest that increase in Re enhances the strength of SPL for all k and St . Higher values of St by increasing oscillation amplitude of the hydrofoil causes growth in magnitudes of the sound pressure levels without appreciably affecting the angular position of the dipole-axis. For some constant Re and St , variations in k has a negligible affect on the sound pressure levels, but it emerges as a significant factor for setting the direction of the dipole-axis. While looking at the plots in a row in figure 10, it becomes apparent that an increase in k revolves the dipole-axis clock-wise.

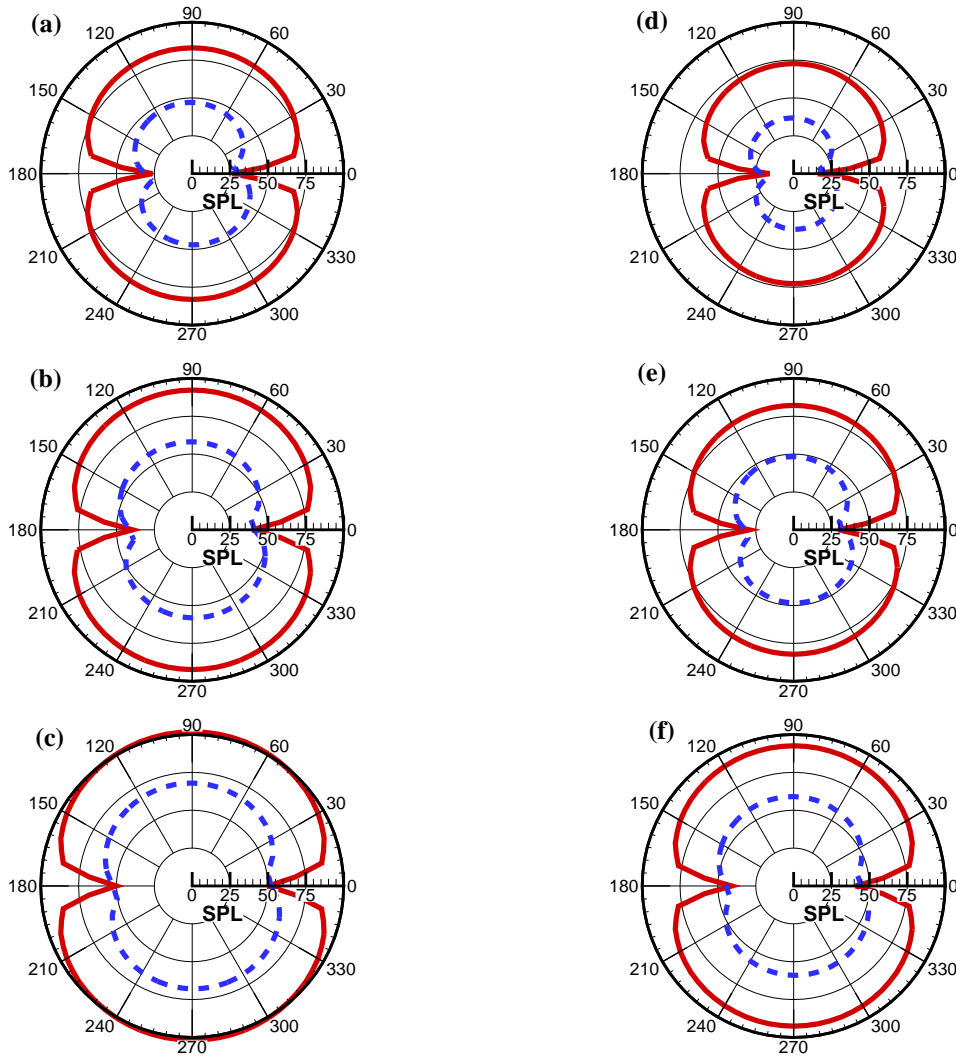


Figure 9. Polar plots for distribution of SPL for $k = 5$ and $St = 0.50$ where the top, middle and bottom rows show data for $Re = 5,000, 10,000$ and $20,000$, respectively. Left and right columns present measurements for SPL at the inner and outer circles, respectively.

3.2. Role of Hydrodynamic Pressure

It is a known fact that sound is propagated through the pressure fluctuations in the surroundings of the noise source. When a solid body oscillates, it causes fluctuation of pressure on its both sides from positive to negative, and vice versa. During an upstroke, the upper surface of the hydrodynamic body appears as the loading side, and experiences positive pressure while displacing the water around. In this case, negative pressure is seen at the lower surface. On the other hand, the signs of the pressure signals get reversed during a down-stroke. These oscillatory pressure quantities are the responsible factors for the flow noise to emit from the body and radiate in the surroundings. Previously, some investigations [8–12] focused towards establishing connections of the

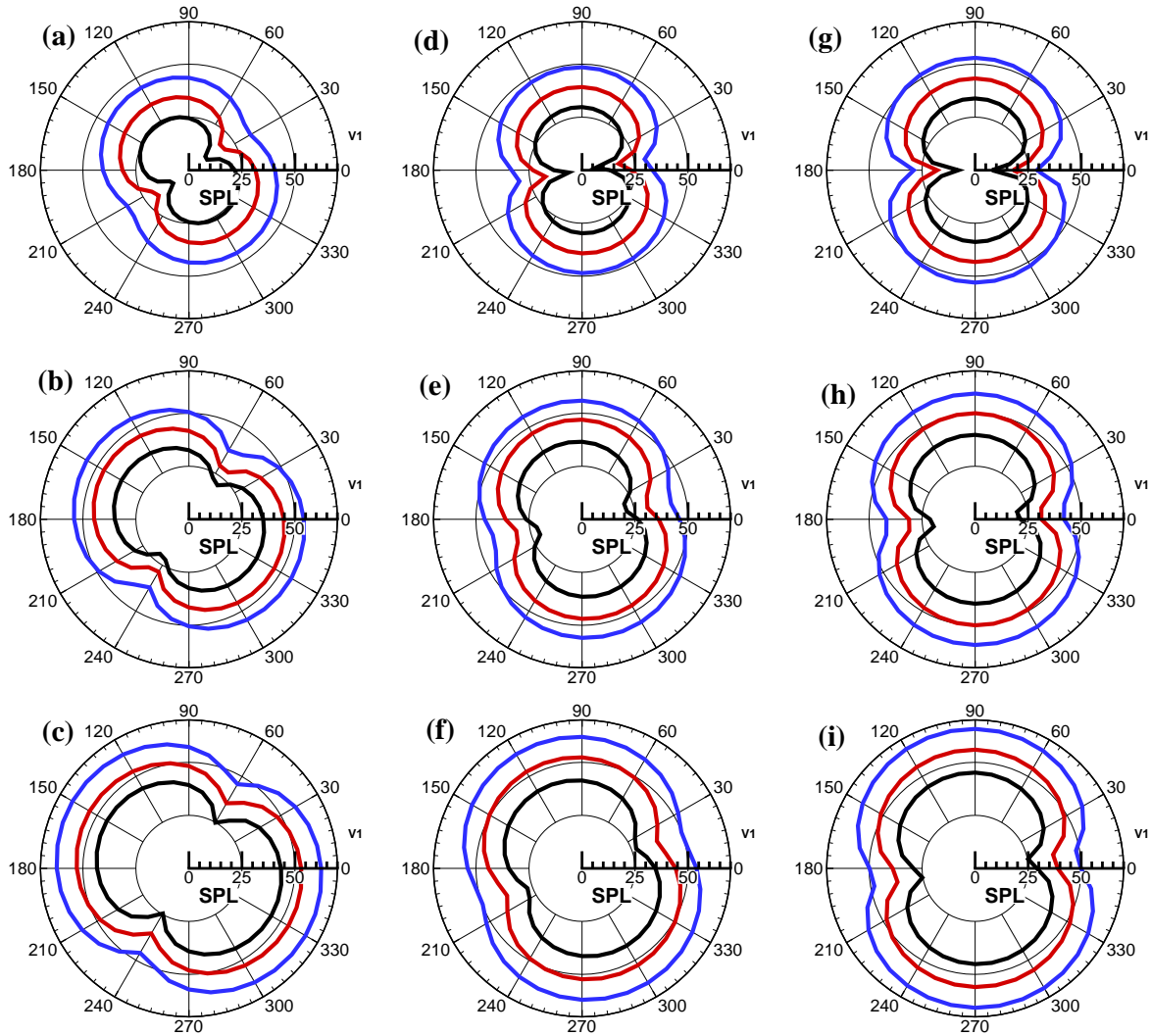


Figure 10. Polar plots for distribution of SPL for $k = 1, 2.5$ and 5 whereas $St = 0.15, 0.30$ and 0.45 . Here the top, middle and bottom rows show data for $St = 0.15, 0.30$ and 0.45 , respectively. Left, middle and right columns present measurements for SPL at $k = 1, 2.5$ and 5 , respectively. Aiming for clarity, we prepare these plots using solid lines, and the readers are referred to the online version for colored figures. In each of these plots, black, blue and red lines show the SPL patterns for $Re = 5,000, 10,000$ and $20,000$, respectively.

SPL distribution patterns with the fluid force coefficients. These coefficients, C_Y and C_D , are presented as the global characteristics to measure pressure perturbations, the loadings on the body, and its hydrodynamic performance. Similarly, we also explore the role of these force coefficients and their associated frequency compositions in the patterns of sound pressure levels. Figure 11 displays the temporal histories and the amplitude spectra for C_Y and C_D . It can be observed that the most dominant frequency in C_Y -spectrum is f_E , whereas it is $2f_E$ in C_D -spectrum. This feature of fish swimming has also been revealed earlier by Khalid et al. [5]. This characteristic clearly explains

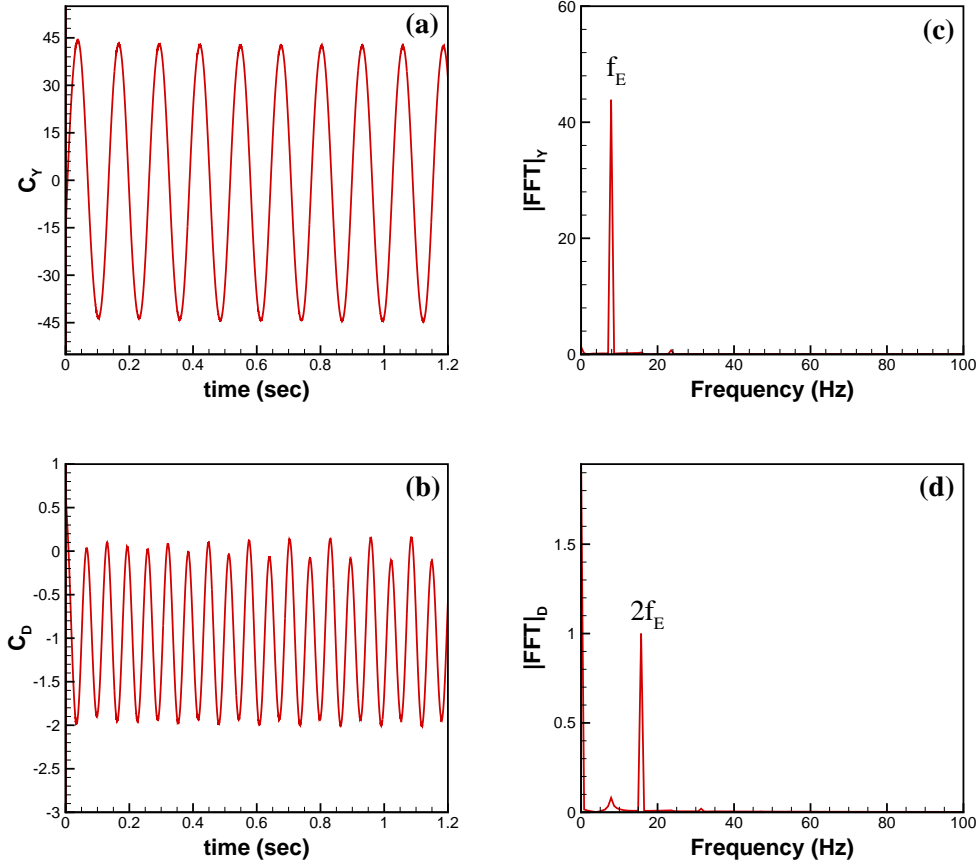


Figure 11. Temporal plots of C_Y and C_D are shown in (a) and (b), respectively, for $\text{Re} = 10,000$, $k = 5$ and $\text{St} = 0.50$. (c) and (d) present the Fourier transforms of both the hydrodynamic force coefficients.

the dominating effect of $2f_E$ in the sound pressure levels along the horizontal direction for the whole range of parameters considered in this study. This observation is also a depiction of the association between the SPL distributions and the hydrodynamic force coefficients.

Next, we aim to analyze the directionality and distribution of SPL in correlation with those of the C_Y and C_D . Following the approach introduced by [12], we project the force coefficient vectors onto the normal directions at each receiver point on the inner circle using the following relation.

$$C_F(\vec{r}, t) = \{C_D(t), C_Y(t)\} \cdot \frac{\vec{r}}{|\vec{r}|} \quad (15)$$

where C_F denotes the hydrodynamic coefficient in the normal direction of an acoustic receiver represented by \vec{r} that initiates from the pitching-axis location. Taking the Fast Fourier transform of C_F and computation of their absolute amplitudes for the frequencies, f_E and $2f_E$, provide us with the patterns shown in figure 12. These polar

plots indicate the dipole-like distribution patterns of the overall hydrodynamic force coefficients for f_E and $2f_E$, and these remain the same for the whole range of parameters considered in this piece of work. It is also interesting to highlight that the dipole-axis for C_F patterns at f_E and $2f_E$ are perpendicular to each other. Here, the dipole-like structures in the left column (figure 12a-c) showing C_F at f_E matches with their corresponding SPL distribution patterns, clearly revealing that both the sound radiation patterns at f_E and their axis correlate with the force coefficients. However, the plots in the right column (figure 12d-f) pose similarity in the distribution patterns with those of the SPL, but the directions of the dipole-axis do not match. Moreover, we also observe that the magnitudes of the C_F patterns stays insensitive to the variations in Re , but SPL dipole-like patterns grow at larger Re . Hence, there exist some additional unknown characteristics responsible for controlling not only the magnitudes of the sound pressure levels, but also their dipole-axes. We intend to explore it further in our future work.

4. Conclusions

In this study, we perform numerical simulations by modeling a moving fish body using a pitching hydrofoil for a range of flow and kinematic parameters. We focus on how these factors affect the radiation of sound in the surrounding water. We seek to find the dependence of the magnitude of the sound pressure levels and the directionality of sound waves through the associated dipole-axes on these governing parameters. Our parametric investigations lead us to the following conclusions. For the whole range of Reynolds number, Strouhal number, and reduced frequency considered in the present study, distributions of sound pressure levels depicting the flow noise around the swimming body present dipole-like radiations patterns for both the oscillation frequency, f_E , and its first even harmonic, $2f_E$. The oscillation frequency dominates in the whole spectrum as compared to $2f_E$ except along the horizontal direction. It is in agreement with the directional strengths of the hydrodynamic forces along the horizontal and sideways directions. As C_D represent the hydrodynamic force in the horizontal direction, and the strongest frequency in its spectra is $2f_E$, we see its dominance in its relevant direction only. Reynolds and Strouhal numbers affect the magnitude of the sound pressure levels. Both of these factors do not seem to control the dipole-axis, and their variations do not show a significant impact in setting its angular position. On the other hand, reduced frequency appears to be the controlling feature for the direction of the dipole-axis. It shows only a minor impact on the magnitude of the SPL levels. Out of all the considered kinematic and flow parameters, Reynolds number comes out to be a potential factor to convert the dipole-like sound radiation pattern into monopole-like ones. There exists a possibility to witness this phenomenon with even higher values of Re that required further inspection. Finally, our current work shows that the fishes and other aquatic animals may control their acoustic signals to their target bodies through adopting certain kinematic features.

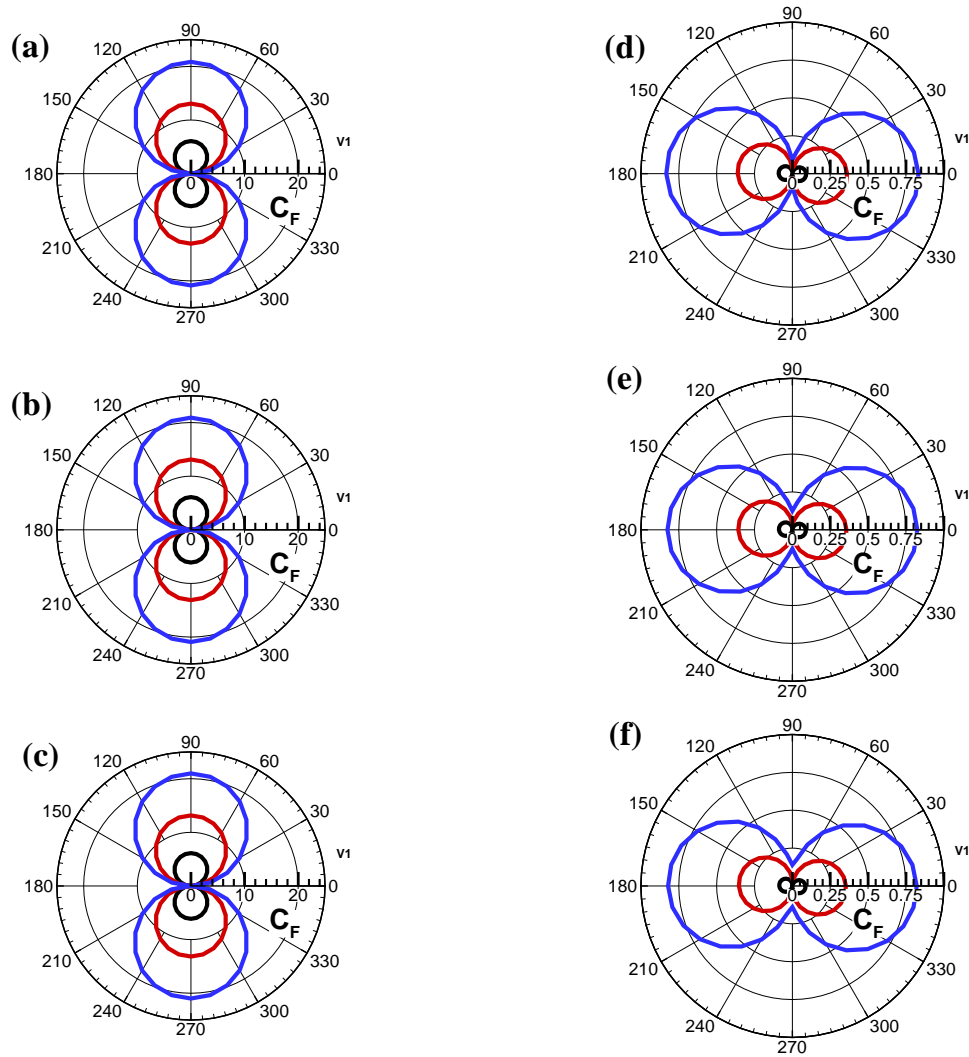


Figure 12. Distribution of total hydrodynamic force coefficients for a range of Re , k and St . Top, middle, and the bottom rows show data for $Re = 5,000$, $10,000$, and $20,000$, respectively. Left and right columns belong to C_F distributions at f_E and $2f_E$, respectively. Black, blue and red lines in each of the figures show patterns for $St = 0.15$, 0.30 and 0.45 , respectively.

Acknowledgments

Dr. Jiang acknowledges the support from the Independent Innovation Fund Project of Agricultural Science and Technology in Jiangsu Province through the Grant No. CX(16)1004, and Key Research and Development Plan of Jiangsu Province (Modern Agriculture) through the Grant No. BE2017334.

References

- [1] Dong H, Bozkurtasi M, Mittal R, Madden P and Lauder G V 2010 *Journal of Fluid Mechanics* **645** 345–373

- [2] Boschitsch B M, Dewey P A and Smits A J 2014 *Physics of Fluids* **26** 051901
- [3] Liu G, Ren Y, Zhu J, Bart-Smith H and Dong H 2015 *Theoretical and Applied Mechanics Letters* **5** 54–57
- [4] Fish F E, Schreiber C M, Moored K W, Liu G, Dong H and Bart-Smith H 2016 *Aerospace* **3** 1–24
- [5] Khalid M S U, Akhtar I and Dong H 2016 *Journal of Fluids and Structures* **66** 19–35
- [6] RSalazar, VFuentes and AAbdelkefi 2018 *Ocean Engineering* **148** 75–114
- [7] Radford C A, Stanley J A and Simpson S D 2011 *Coral Reefs* **30** 295–305
- [8] Sueur J, Tuck E J and Robert D 2005 *The Journal of the Acoustical Society of America* **118** 530–538
- [9] Bae Y and Moon Y J 2008 *The Journal of the Acoustical Society of America* **124** 72–81
- [10] Inada Y, Aono H, Liu H and Aoyama T 2009 *Theoretical and Applied Mechanics Japan* **57** 437–447
- [11] Lu Z, Debiasi M, Nguyen Q V and Chan W L 2016 An experimental investigation on the acoustic performance of a flapping wing micro-air-vehicle (Melbourne, Australia: Inter-noise 2014)
- [12] Geng B, Xue Q, Zheng X, Liu G, Ren Y and Dong H 2018 *Bioinspiration & Biomimetics* **13** 016010
- [13] Saadat M, Fish F E, Domel A G, Santo V D, Lauder G V and Haj-Hariri H 2017 *Physical Review Fluids* **2** 083102
- [14] Ansys 2015 *Fluent 16.1 Userguide* ANSYS Inc.
- [15] Kinsey T and Dumas G 2008 *AIAA Journal* **46** 1318–1330
- [16] Ashraf M A, Young J and Lai J C S 2011 *Journal of Fluids and Structures* **27** 145–160
- [17] Kinsey T and Dumas G 2014 *AIAA Journal* **52** 1885–1895
- [18] The J and Yu H 2017 *Energy* **138** 257–289
- [19] Kinsey T and Dumas G 2012 *Journal of Fluids Engineering* **134** 021104
- [20] Kinsey T and Dumas G 2012 *Journal of Fluids Engineering* **134** 031103
- [21] Kinsey T and Dumas G 2012 *Journal of Fluids Engineering* **134** 071105
- [22] Ashraf M A, Young J and Lai J C S 2012 *AIAA Journal* **52** 2308–2324
- [23] Ffowcs-Williams J E and Hawkins D L 1969 *Philosophical Transactions of The Royal Society A Mathematical Physical and Engineering Sciences* **264**
- [24] Lighthill M J 1952 *Proceedings of Royal Society of London Series A: Maths and Physical Sciences* **211** 564–587
- [25] Mohamed M H 2016 *Energy* **96** 531–544
- [26] Ghasemian M and Nejat A 2015 *Energy* **88** 711–717
- [27] Mohamed M H 2014 *Energy* **65** 596–604